Beyond the Rayleigh scattering limit in high-Q silicon microdisks: theory and experiment

Matthew Borselli, Thomas J. Johnson, and Oskar Painter

Department of Applied Physics, California Institute of Technology, Pasadena, CA 91125, USA.

borselli@caltech.edu

http://copilot.caltech.edu

Abstract: Using a combination of resist reflow to form a highly circular etch mask pattern and a low-damage plasma dry etch, high-quality-factor silicon optical microdisk resonators are fabricated out of silicon-on-insulator (SOI) wafers. Quality factors as high as $Q = 5 \times 10^6$ are measured in these microresonators, corresponding to a propagation loss coefficient as small as $\alpha \sim 0.1$ dB/cm. The different optical loss mechanisms are identified through a study of the total optical loss, mode coupling, and thermally-induced optical bistability as a function of microdisk radius (5-30 μm). These measurements indicate that optical loss in these high-Q microresonators is limited not by surface roughness, but rather by surface state absorption and bulk free-carrier absorption.

OCIS codes: (230.5750) Resonators; (190.1450) Bistability; (190.4870) Optically induced thermo-optical effects;

References and links

1. L. Pavesi and D. Lockwood, *Silicon Photonics* (Springer-verlag, New York, 2004).
2. G. Reed and A. Knights, *Silicon Photonics: An Introduction* (John Wiley, West Sussex, 2004).
3. A. Liu, R. Jones, L. Liao, D. Samara-Rubio, D. Rubin, O. Cohen, R. Nicolaescu, and M. Paniccia, "A high-speed silicon optical modulator based on a metal-oxide-semiconductor capacitor," Nature **427**, 615–618 (2004).
4. V. R. Almeida, C. A. Barrios, R. R. Panepucci, and M. Lipson, "All-optical control of light on a silicon chip," Nature **431**, 1081–1084 (2004).
5. O. Boyraz and B. Jalali, "Demonstration of a silicon Raman laser," Opt. Express **12**, 5269–5273 (2004), http://www.opticsexpress.org/abstract.cfm?URI=OPEX-12-21-5269.
6. H. Rong, R. Jones, A. Liu, O. Cohen, D. Hak, A. Fang, and M. Paniccia, "A continuous-wave Raman silicon laser," Nature **433**, 725–728 (2005).
7. K. Okamoto, *Fundamentals of optical waveguides* (Academic Press, San Diego, 2000).
8. B. E. Little, "A VLSI Photonics Platform," in *Optical Fiber Communication Conference* (2003).
9. M. Borselli, K. Srinivasan, P. E. Barclay, and O. Painter, "Rayleigh scattering, mode coupling, and optical loss in silicon microdisks," Appl. Phys. Lett. **85**, 3693–3695 (2004).
10. D. W. Vernooy, V. S. Ilchenko, H. Mabuchi, E. W. Streed, and H. J. Kimble, "High-Q measurements of fused-silica microspheres in the near infrared," Opt. Lett. **23**, 247–249 (1998).
11. M. Cai, O. Painter, and K. Vahala, "Observation of critical coupling in a fiber taper to a silica-microsphere whispering-gallery mode system," Phys. Rev. Lett. **85**, 74–77 (2000).
12. D. K. Armani, T. J. Kippenberg, S. M. Spillane, and K. J. Vahala, "Ultra-high-Q toroid microcavity on a chip," Nature **421**, 925–928 (2003).
13. E. Yablonovitch, D. L. Allara, C. C. Chang, T. Gmitter, and T. B. Bright, "Unusually Low Surface-Recombination Velocity on Silicon and Germanium Surfaces," Phys. Rev. Lett. **57**, 249–252 (1986).
14. K. Srinivasan, P. E. Barclay, M. Borselli, and O. Painter, "Optical-fiber-based measurement of an ultrasmall volume, high-Q photonic crystal microcavity," Phys. Rev. B **70**, 081306(R) (2004).

#6513 - $15.00 US Received 2 February 2005; revised 21 February 2005; accepted 22 February 2005

15. M. Haverlag, D. Vender, and G. S. Oehrlein, "Ellipsometric study of silicon surface damage in electron cyclotron resonance plasma etching using CF_4 and SF_6," Appl. Phys. Lett. **61**, 2875–2877 (1992).
16. P. E. Barclay, K. Srinivasan, and O. Painter, "Nonlinear response of silicon photonic crystal microresonators excited via an integrated waveguide and a fiber taper," Opt. Express **13**, 801–820 (2005), http://www.opticsexpress.org/abstract.cfm?URI=OPEX-13-3-801.
17. S. Spillane (2004). Private communication.
18. D. Weiss, V. Sandoghdar, J. Hare, V. Lefévre-Seguin, J. Raimond, and S. Haroche, "Splitting of high-*Q* Mie modes induced light backscattering in silica microspheres," Opt. Lett. **22**, 1835–1837 (1995).
19. B. E. Little, J.-P. Laine, and S. T. Chu, "Surface-Roughness-Induced Contradirectional Coupling in Ring and Disk Resonators," Opt. Lett. **22**, 4–6 (1997).
20. M. Gorodetsky, A. Pryamikov, and V. Ilchenko, "Rayleigh scattering in high-Q microspheres," J. Opt. Soc. Am. B **17**, 1051–1057 (2000).
21. T. J. Kippenburg, S. M. Spillane, and K. J. Vahala, "Modal coupling in traveling-wave resonators," Opt. Lett. **27**, 1669–1671 (2002).
22. B. E. Little and S. T. Chu, "Estimating surface-roughness loss and output coupling in microdisk resonators," Opt. Lett. **21**, 1390–1392 (1996).
23. A. Yariv, *Optical Electronics*, 4th ed. (Saunder College Publishing, a division of Holt, Rinehart and Winston, Inc., Orlando, Florida, 1991).
24. M. Kuznetsov and H. A. Haus, "Radiation Loss in Dielectric Waveguide Structures by the Volume Current Method," IEEE J. Quan. Elec. **19**, 1505–1514 (1983).
25. R. A. Soref and B. R. Bennett, "Electrooptical effects in silicon," IEEE J. Quan. Elec. **23**, 123–129 (1987).
26. V. R. Almeida and M. Lipson, "Optical bistability on a silicon chip," Opt. Lett. **29**, 2387–2389 (2004).
27. H. Rokhsari, S. M. Spillane, and K. J. Vahala, "Loss characterization in microcavities using the thermal bistability effect," Appl. Phys. Lett. **85**, 3029–3031 (2004).
28. S. M. Spillane, T. J. Kippenberg, O. J. Painter, and K. J. Vahala, "Ideality in a fiber-taper-coupled microresonator system for application to cavity quantum electrodynamics," Phys. Rev. Lett. **91**, 043,902 (2003).
29. J. D. Joannopoulos, R. D. Meade, and J. N. Winn, *Photonic Crystals* (Princeton University Press, Princeton, New Jersey, 1995).
30. H. A. Haus, *Waves and Fields in Optoelectronics*, 1st ed. (Prentice-Hall, Englewood Cliffs, New Jersey 07632, 1984).

1. Introduction

Silicon (Si) photonics has received renewed interest of late due to the rapidly approaching limits of "Moore's Law" scaling in Si microelectronics, and the potential to leverage the near half-century of processing development in the microelectronics industry [1, 2]. There has followed several recent advances in Si optoelectronics, among them the demonstrations of a high-speed Si optical modulator ($>$ 1 Gbit/sec [3]), an all-optical high-speed switch [4], and a nonlinear optical Si laser source based on the stimulated Raman effect [5, 6]. Aiding in these and previous developments of integrated optical and electronic Si circuits is the availability of high index contrast silicon-on-insulator (SOI) wafers, which provide the tight optical confinement of light necessary for high-density optoelectronic integration and nonlinear optics, and exceptional photonic and electronic isolation through the high quality underlying thermal oxide. As Si microphotonic device functionality and integration advances, and light is more often routed into the Si, it will be important to develop low-loss Si microphotonic circuits in addition to the already low-loss glass-based Planar Lightwave Circuits (PLCs) [7, 8]. One key element in such circuits is the microresonator, where light can be distributed by wavelength or localized to enhance nonlinear interactions. Here we report advances in silicon microfabrication which have allowed the creation of SOI-based microdisk optical resonators [9] with extremely smooth high-index-contrast etched sidewalls. These microdisks provide tight optical confinement down to microdisk radii of 1.5 μm, while maintaining the low loss of the high-purity crystalline silicon. Resonant mode quality factors as high as $Q \sim 5 \times 10^6$ are measured, corresponding to an effective propagation loss as small as $\alpha \sim 0.1$ dB/cm.

Inspired by the ultra-smooth glass microspheres [10, 11] and microtoroids [12] formed under surface tension, in this work an electron-beam resist reflow technique is used to significantly reduce surface imperfections in the edge of the microdisk resonator. A fiber-based, wafer-scale

#6513 - $15.00 US Received 2 February 2005; revised 21 February 2005; accepted 22 February 2005

probing technique is used to rapidly and non-invasively test the optical properties of these fabricated microdisks. After a brief description of the fabrication and measurement technique, a comprehensive analysis of the different optical loss mechanisms in these structures is presented below, with a detailed theoretical treatment in the appendices. These measurements indicate that with the reduced level of microdisk surface roughness, we are in fact quantitatively probing the absorption of the surface-states at the edge of the disk (for smaller microdisks) and the bulk Si free-carrier absorption due to ionized dopants (for larger microdisks). Owing to the high finesse of the Si microdisks, the input pump powers required to observe even extremely weak nonlinearities such as two-photon absorption (TPA) and Raman scattering is reduced to the microwatt level. In what follows we study the low power thermally-induced optical bistability, including the distortion effects of TPA and free-carrier absorption (FCA), as a second, more direct, measure of the linear absorption component of the optical loss. These measurements indicate that for further reduction in the optical loss of high-index contrast Si structures, such as the microdisks studied here, new passivation and annealing techniques, analogous to those used in the manufacture of high-quality Si CMOS devices [13], will need to be developed.

2. Fabrication and measurement technique

The silicon microdisks characterized in this work are fabricated from a silicon-on-insulator (SOI) wafer with 344 nm thick p-doped Si device layer on a 2 μm SiO_2 layer (Fig. 1(c)). Processing of the microdisks begins with the deposition of a 20 nm SiO_2 protective cap layer using plasma-enhanced chemical-vapor-deposition. An electron-beam resist, Zeon®ZEP520A, is spin-coated onto the wafer at 6000 rpm for 60 sec, resulting in a 400 nm thick film. Disks of radii ranging from $5-30$ μm are defined in the electron-beam resist. The wafer is then subjected to a post-lithography bake. By suitable choice of temperature and duration, this bake can significantly reduce imperfections in the electron-beam resist pattern. Temperatures too low do not result in resist reflow, while temperatures too high can cause significant loss of resist to sublimation. A temperature high enough to allow the resist to reflow must be reached and maintained for the imperfections in the resist pattern to be reduced. The appropriate duration and temperature for the resist prepared as described above was empirically determined to be 5 minutes at 160°C. After the reflow process, the roughness in the patterns is greatly reduced, and the sidewall angle is reduced from 90° to approximately 45°. The resulting angled mask is prone to erosion during the etch process, and so the inductively-coupled-plasma reactive-ion etch is optimized to minimize roughness caused by mask erosion.

The patterns are then transferred into the Si device layer using a low DC-bias, inductively-coupled-plasma reactive-ion etch with SF_6/C_4F_8 chemistry [14, 15]. To enable optical fiber probing of the devices (as described below), an etch-mask surrounding the disks is photolithographically defined and the wafer surrounding the disks etched down several microns, leaving the devices isolated on a mesa. Following a Piranha etch to remove organic materials, a dilute hydrofluoric acid solution is used to remove the protective SiO_2 layer and partially undercut the disk (Fig. 1(c)). The undercut pedestal takes on its angular hour-glass shape due to a higher etch rate on the wafer Unibond®[2] versus the bulk silica. The wafer is then rinsed in deionized water and dried with clean, dry N_2. Upon completion of the processing, the wafer is immediately removed to an N_2 purged enclosure for characterization.

To characterize the microdisk resonators an evanescent fiber taper coupling technique is employed [9, 14]. In this process, an optical fiber is adiabatically drawn to a $1-2$ μm diameter using a hydrogen torch so that its evanescent field is made accessible to the environment. Using DC motor stages with 50 nm encoded resolution, the fiber taper can be accurately positioned within the microdisk near-field so as to evanescently couple power into the microdisks. Measurements of the taper transmission as a function of the taper-microdisk gap and

#6513 - $15.00 US Received 2 February 2005; revised 21 February 2005; accepted 22 February 2005

input power are performed using swept wavelength tunable laser sources ($\lambda = 1410$-1625 nm, linewidth < 5 MHz). A set of paddle wheels is used to adjust the polarization state of the fiber taper mode in the microdisk coupling region, providing selective coupling to the TE-like (TM-like) whispering gallery modes (WGMs) with dominant electric field parallel (normal) to the plane of the microdisk. Further details of the fiber taper apparatus and measurement techniques can be found in Refs. [16, 14].

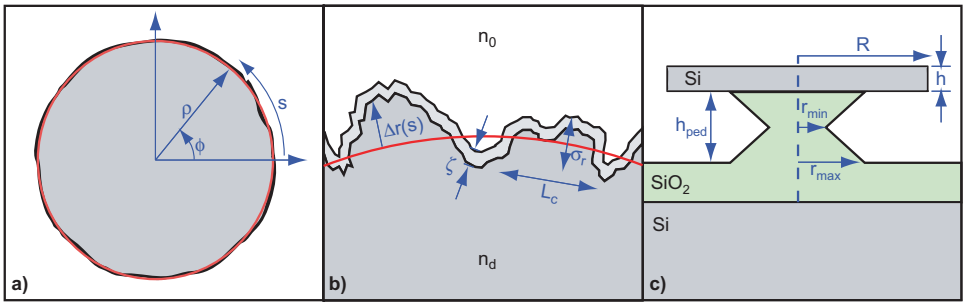

Fig. 1. Schematic representation of a fabricated silicon microdisk. (a) Top view showing ideal disk (red) against disk with roughness. (b) Top view close-up illustrating the surface roughness, $\Delta r(s)$, and surface reconstruction, ζ. Also shown are statistical roughness parameters, σ_r and L_c, of a typical scatterer. (c) Side view of a fabricated SOI microdisk highlighting idealized SiO_2 pedestal.

3. Experimental results and analysis

In order to study the optical loss mechanisms within the Si microdisk resonators, a series of disks with radii, $R = 5, 10, 15, 20, 30\ \mu$m, was created. The *intrinsic* optical loss in these structures can be quantified by four different components of a modal quality factor, Q_i, according to

$$1/Q_i = 1/Q_r + 1/Q_{ss} + 1/Q_{sa} + 1/Q_b, \tag{1}$$

where Q_r, Q_{ss}, Q_{sa}, Q_b are related to optical loss due to radiation, surface scattering, surface absorption, and absorption in the bulk Si, respectively. Due to the near ideal nature of the optical confinement of the silicon whispering-gallery-mode (WGM) resonator, the radiation losses become increasingly negligible as the disk radius is increased ($Q_r \gtrsim 10^8$ for $R > 1.5\ \mu$m [17]). While all of the disks considered in this work possess inconsequential radiation losses, the better radial confinement of larger radii microdisks pulls the WGMs away from the disk edge, as described in Appendix E. Thus, varying the disk radius provides a means to separate sidewall surface effects, quantified by Q_{ss} and Q_{sa}, from bulk effects, Q_b.

A typical taper transmission spectrum of an $R = 30\ \mu$m microdisk is shown in Fig. 2. The observed double resonance dip (doublet) is a result of Rayleigh scattering from disk surface roughness, illustrated in Fig. 1(b) as $\Delta r(s)$. The surface imperfections created during fabrication lift the degeneracy of clockwise (cw) and counter-clockwise (ccw) propagating WGMs in the microdisk, creating instead standing wave modes [18, 19, 20, 21]. As described in Ref. [9], the highest Q WGMs in these microdisks are found to be of TM-like polarization and of radial mode number $n = 1$, where the field interaction with the disk-edge surface is minimized (see Appendices). For the wavelengths studied here, the corresponding azimuthal number is $M \sim 60$ for the $R = 5\ \mu$m disks, and scales approximately linearly with radius for larger microdisks. All of the WGMs studied in this work were confirmed to be of TM-like polarization and of radial

#6513 - $15.00 US Received 2 February 2005; revised 21 February 2005; accepted 22 February 2005

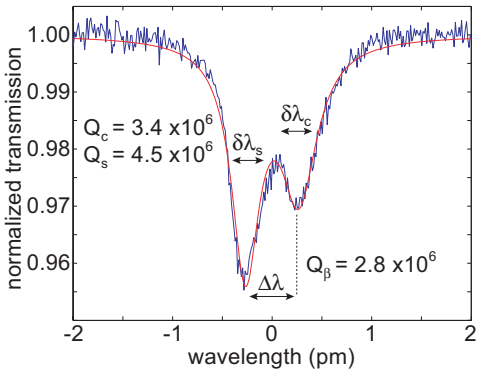

Fig. 2. Taper transmission versus wavelength showing a high-Q doublet mode for the $R = 30$ μm disk. $Q_c \equiv \lambda_0/\delta\lambda_c$ and $Q_s \equiv \lambda_0/\delta\lambda_s$ are the unloaded quality factors for the long and short wavelength modes respectively, where $\delta\lambda_c$ and $\delta\lambda_s$ are resonance linewidths. Also shown is the doublet splitting, $\Delta\lambda$, and normalized splitting quality factor, $Q_\beta \equiv \lambda_0/\Delta\lambda$.

number $n \sim 1$ through studies of their polarization and position dependent coupling to the fiber taper [9].

A statistical model for the doublet splitting is constructed using the effective index model from Appendix A and the time dependent perturbation theory described in Appendix C. The resulting model [20, 21] is used to fit the data in Fig. 2 with linewidth parameters, $\delta\lambda_c$ and $\delta\lambda_s$, and doublet splitting, $\Delta\lambda$. Two independent linewidth parameters must be used because the resulting orthogonal standing wave modes sense different regions of the disk surface [21]. A normalized measure of the mode splitting is defined to be the free-space wavelength, λ_0, divided by the *total* resonance splitting ($\Delta\lambda$), given here by Q_β. To illustrate the utility of this defintion, limiting cases are taken: $Q_\beta \gg Q_i$ would indicate no doublet splitting and pure *cw* and *ccw* traveling WGMs; conversely, $Q_\beta \ll Q_i$ would indicate large doublet splitting and consequently widely separated standing wave WGMs. In the latter case, Q_β gives a better measure of the required coupling strength and the useful bandwidth at *critical coupling*, where all power is transferred into the resonant cavity from a bus waveguide (see inset to Fig. 3).

Figure 3 plots Q_β for each of the measured microdisk radii, where for each microdisk we plot the results for the four highest Q_i doublet modes in the 1410-1500 nm wavelength range. Combining the results of Appendix C with an approximate form for disk edge energy density (see Appendix E), we get the following equation for the normalized doublet splitting parameter:

$$Q_\beta \equiv \frac{\lambda_0}{\Delta\lambda} = \frac{1}{\sqrt{2}\pi^{3/4}\xi}\left(\frac{V_d}{V_s}\right), \tag{2}$$

where V_d is simply the physical volume of the microdisk and ξ is the relative dielectric contrast constant defined as

$$\xi = \frac{\bar{n}^2\left(n_d^2 - n_0^2\right)}{n_d^2\left(\bar{n}^2 - n_0^2\right)}. \tag{3}$$

$n_d \sim 3.55$, $n_0 = 1.0$, and $\bar{n}$ are the indices of refraction for the silicon disk, cladding, and 2-D effective slab, respectively [22, 23]. The key parameter from this analysis is the effective volume of a typical scatterer, defined as $V_s \equiv \sqrt{RL_c}h\sigma_r$, where L_c is the correlation length of the roughness, h is the disk height, and σ_r is the standard deviation of the roughness amplitude

#6513 - $15.00 US Received 2 February 2005; revised 21 February 2005; accepted 22 February 2005

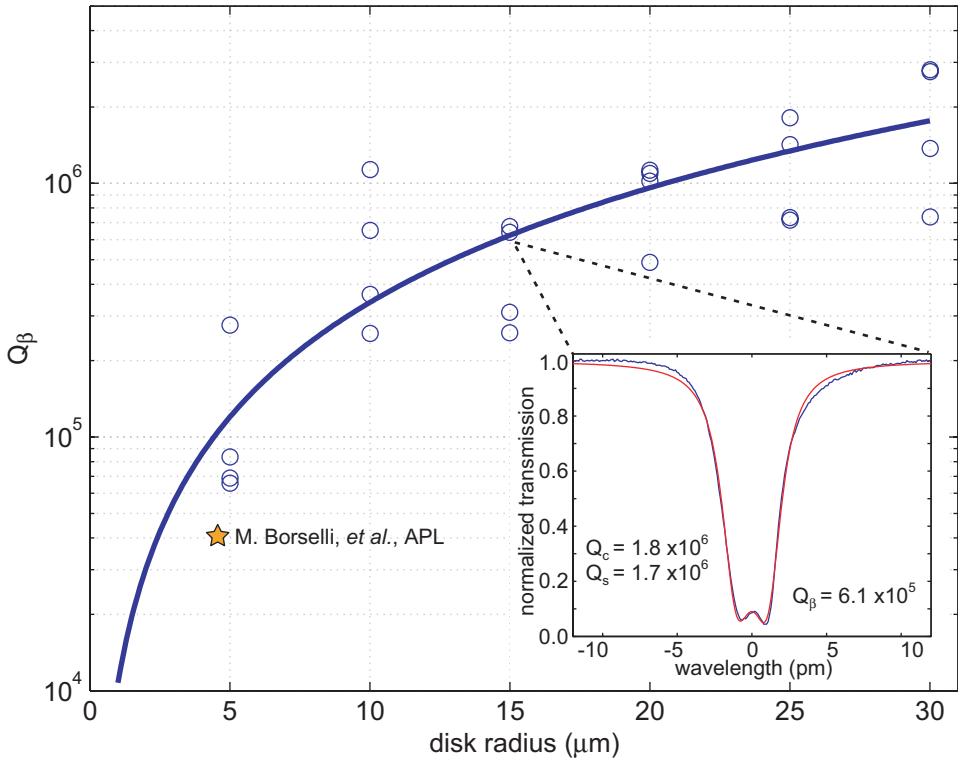

Fig. 3. Normalized doublet splitting (Q_β) versus disk radius. (inset) Taper transmission data and fit of deeply coupled doublet demonstrating 14 dB coupling depth.

(illustrated in Fig. 1(b)). Fitting the doublet splitting versus disk radius in Fig. 3 (solid blue curve) to the $Q_\beta \sim R^{3/2}$ dependence shown in Eq. (2), gives a value of $\sqrt{L_c}\sigma_r = 2.7$ nm$^{3/2}$. This parameter is also useful in estimating optical loss because the same Rayleigh scattering mechanism responsible for lifting the azimuthal degeneracy couples the unperturbed microdisk modes to radiation modes [24, 20].

From an analysis similar to that used for the mode coupling, the surface scattering quality factor, Q_{ss}, is approximated as (see Appendix B):

$$Q_{ss} = \frac{3\lambda_0^3}{8\pi^{7/2} n_0 \delta n^2 \xi} \left(\frac{V_d}{V_s^2}\right), \tag{4}$$

where $\delta n^2 \equiv n_d^2 - n_0^2$. Figure 4 plots the measured linewidths ($\delta\lambda_{c,s}$) of each of the microdisk modes represented in Fig. 3 as a dimensionless quality factor, $Q_i \equiv \lambda_0/\delta\lambda_{c,s}$ (shown as black circles, one for each mode of a doublet pair). From Eq. (4), we see that the model of Appendix B yields a linear dependence versus disk radius of the surface scattering quality factor, Q_{ss}. The dash-dotted blue curve shown in Fig. 4 represents the resulting surface scattering component of the total loss as predicted by the fit to $\sqrt{L_c}\sigma_r$ from the observed doublet splitting. In comparison to recently reported results not incorporating the e-beam resist reflow technique [9] (shown as an * in Figs. 3 and 4), the doublet splitting has been reduced by nearly a factor of 2.5. This results in an increase in the predicted Q_{ss} by more than a factor of 6. Given that the measured quality factor of the current microdisk resonators has only doubled, this suggests that our new work is limited by loss mechanisms not significant in previous work [9].

#6513 - $15.00 US Received 2 February 2005; revised 21 February 2005; accepted 22 February 2005

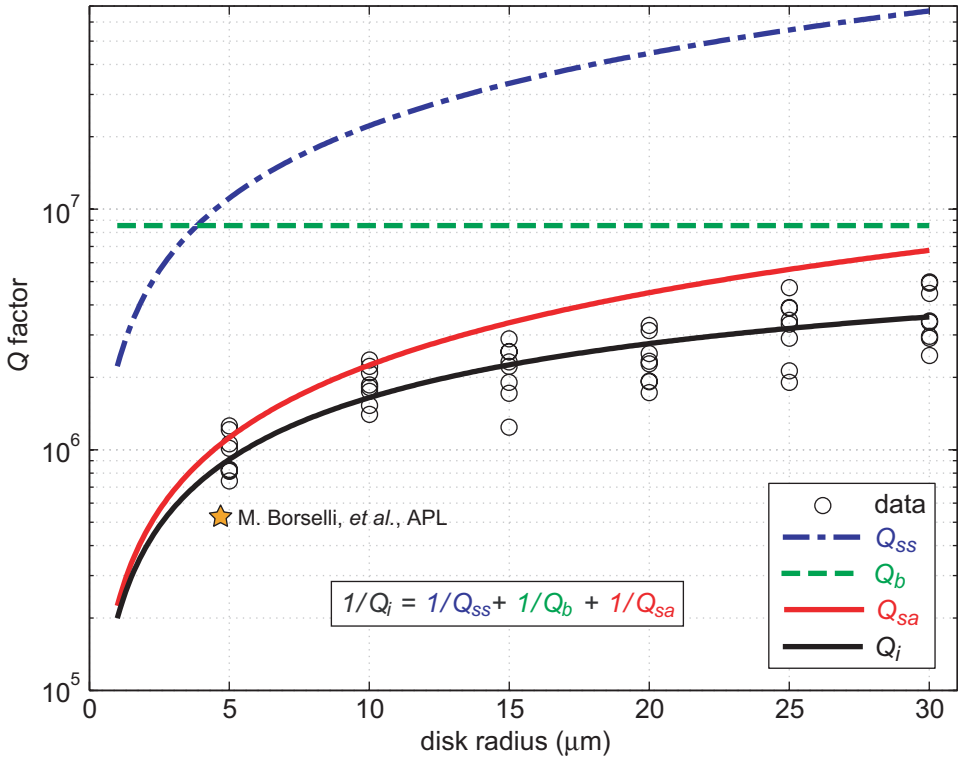

Fig. 4. Measured intrinsic quality factor, Q_i, versus disk radius and resulting breakdown of optical losses due to: surface scattering (Q_{ss}), bulk doping and impurities (Q_b), and surface absorption (Q_{sa}).

Subtracting the fit to Q_{ss} from the data, a strong linear dependence with radius still remains. Since the optical losses decrease as the modes are pulled in toward the center of the microdisk, we assume that neither the pedestal nor the top and bottom surfaces are significant sources of optical loss. As shown in Appendix D, a disk edge surface absorption component of optical loss would have a linear dependence with microdisk radius, similar to that of surface scattering. The approximate dependence of the surface absorption quality factor, Q_{sa}, is found in the analysis from Appendix D to be given as:

$$Q_{sa} = \frac{\pi c \left(\bar{n}^2 - n_0^2\right) R}{\lambda_0 \bar{n}^2 \gamma_{sa} \zeta}, \tag{5}$$

where γ_{sa} is the bulk absorption rate of a material consisting entirely of that at the microdisk surface. As schematically illustrated in Fig. 1(b), we propose that the dominant form of surface absorption occurs at the edge of the microdisk along the etched sidewalls, where reactive ion etch damage of the Si lattice can result in a reconstruction depth, ζ, for many monolayers [15]. Fitting the remaining unaccounted for optical loss (i.e., subtracting out the predicted surface scattering component) versus microdisk radius with a linear (Q_{sa}, solid red curve) and constant (Q_b, dashed green curve) component, we arrive at the plot shown in Fig. 4. From this fit we find that our microdisks are limited to a $Q_b \cong 8.5 \times 10^6$. Using resistivity measurements from the manufacturer of the boron doped SOI material used in this work ($1-3\ \Omega$·cm) and silicon absorption studies [25], residual free carriers in our material should limit $Q_b \lesssim (3.7-8.8 \times$

#6513 - $15.00 US Received 2 February 2005; revised 21 February 2005; accepted 22 February 2005

10^6), consistent with our analysis.

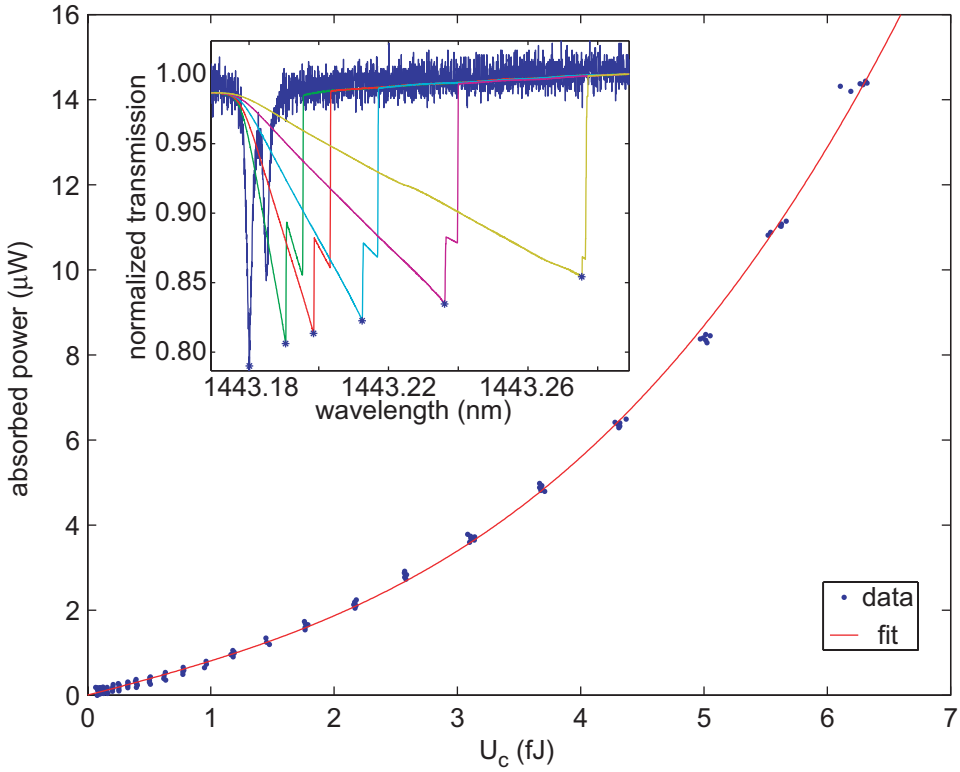

Fig. 5. Plot showing absorbed power versus intra-cavity energy for a $R = 5$ μm disk to deduce linear, quadratic, and cubic loss rates. (inset) normalized data selected to illustrate bistability effect on resonance.

To corroborate the above surface absorption conclusions, a series of power dependent experiments was performed. The small SiO_2 pedestal ($r_{max} \cong 2.5$ μm, $r_{min} \cong 1$ μm, $h_{ped} \cong 1.2$ μm) in the $R = 5$ micron microdisk presented here provides relatively poor thermal contact as compared to the larger radii disks. As a result, thermally-induced shifts in resonant mode wavelengths (inset to Fig. 5) provide a sensitive measure of internal cavity absorption [26, 27, 16]. As the input power to the microdisk is increased, the change in resonance wavelength from the "cold-cavity" position can be related to absorbed power inside the microdisk, P_{abs}. Since the thermal conductivity of silicon is roughly 100 times greater than that of silica, the steady-state temperature inside the silicon disk is constant (disregarding the neglible heat flow to the ambient N_2 environment). Furthermore, the remaining buried oxide and silicon substrate, being several orders of magnitude larger in cross-section than the pedestal, can be assumed to act as a thermal bath of constant temperature. These assumptions reduce the thermal behavior of the microresonator to a time-independent, one-dimensional heat flow problem, depending primarily on the geometry of the pedestal.

The thermal resistance, R_{th}, of the narrow pedestal can be calculated from the thermal conductivity of thermal oxide ($\kappa_{SiO_2} \sim 1.38$ W·K^{-1}m^{-1}) and the geometry of the pedestal (shown schematically in Fig. 1(c)):

$$R_{th} = h_{ped} \,/\, (\kappa_{SiO_2} \pi r_{max} r_{min}). \tag{6}$$

#6513 - $15.00 US
Received 2 February 2005; revised 21 February 2005; accepted 22 February 2005

The change in resonance wavelength can then be approximately related to the optical power absorbed via the linear relationships

$$\Delta\lambda_0 \overset{n_{\mathrm{Si}}/\lambda_0}{\Longrightarrow} \Delta n \overset{(dn/dT)_{\mathrm{Si}}^{-1}}{\Longrightarrow} \Delta T \overset{R_{th}^{-1}}{\Longrightarrow} P_{\mathrm{abs}}, \tag{7}$$

where the thermo-optic coefficient of Si is denoted by $(dn/dT)_{\mathrm{Si}} \sim 1.5\times10^{-4}$ K^{-1}[16]. We finally arrive at the working equation relating the wavelength shift seen in the inset to Fig. 5 to the absorbed power:

$$P_{\mathrm{abs}} = \frac{\kappa_{\mathrm{SiO_2}}\pi r_{\mathrm{max}} r_{\mathrm{min}} n_{\mathrm{Si}}}{h_{\mathrm{ped}}\left.\frac{dn}{dT}\right|_{\mathrm{Si}}\lambda_0}\Delta\lambda_0. \tag{8}$$

To calculate the linear absorption rate, the internal cavity energy must also be found from the minima in the normalized transmission spectra, T_{min}, and input power, P_{in}. Under steady-state conditions, conservation of power requires that the power dropped into the cavity, $P_d = (1-T_{\mathrm{min}})P_{in}$, be equal to the power lost out of the cavity-waveguide system, P_L. From the formal definition of *intrinsic* quality factor, Q_i', we can relate the cavity energy to the power loss by

$$U_c = \frac{Q_i'}{\omega}P_L = \frac{Q_i'}{\omega}(1-T_{\mathrm{min}})P_{in}, \tag{9}$$

where ω is the optical frequency and U_c is the internal cavity energy. Taking into account the external loading from the fiber taper, the total observed quality factor (linewidth) can be written as $1/Q_t = 1/Q_e + 1/Q_i'$, where Q_e relates to the coupling of optical power from the fiber taper to the microdisk. Q_i' in this case includes all intrinsic loss of the microdisk resonator and any additional parasitic loading from the fiber taper. As the resonant mode linewidth cannot be directly measured at high powers (due to nonlinear distortion), it must be inferred from the depths of transmission and the "cold-cavity" linewidth [16]. Using a simple model for the waveguide-resonator system [28], we can find Q_e by measuring the total linewidth at *low* powers and using the relation $Q_e = 2Q_t/(1-\sqrt{T_{\mathrm{min}}})$. One can then show that $Q_i' = Q_e(1-\sqrt{T_{\mathrm{min}}})/(1+\sqrt{T_{\mathrm{min}}})$ for *all* powers, assuming that the taper loading does not change with input power. With complete knowledge of Q_e and Q_i', we can finally determine the internal cavity energy versus input power.

Figure 5 shows a typical data set for the power dependent absorption effects for the $R = 5$ μm microdisk modes previously described for Figs 3 and 4. At low powers, P_{abs} scales linearly with U_c, while at higher powers, the onset of two-photon absorption (quadratic term) and free-carrier absorption (cubic term) become readily apparent. A cubic polynomial fit ($P_{\mathrm{abs}} \sim aU_c^3 + bU_c^2 + \gamma_{\mathrm{lin}}U_c$) for the four $R = 5$ μm modes yields a linear absorption quality factor of $Q_{\mathrm{lin}} \equiv \omega/\gamma_{\mathrm{lin}} = (1.5\pm0.3)\times10^6$. This value is in very good agreement with the estimated Q_{sa} from the analysis above (solid red curve in Fig. 4). Also, as the measurements of the modes in the larger microdisks have significantly higher measured Q_i than the measured Q_{lin}, this is a strong indication that we are indeed quantitatively probing the surface state absorption and not the bulk absorption for the smaller $R = 5$ μm microdisks.

4. Conclusion

Using a combination of resist reflow to form a surface-tension limited smooth etch mask and a low DC bias dry etch to reduce roughness and damage in the etched Si sidewalls, we have fabricated high-index contrast Si microdisk microresonators with strong optical confinement and losses as low as 0.1 dB/cm ($Q > 5\times10^6$). Passive fiber optic measurements of the scaling

#6513 - $15.00 US Received 2 February 2005; revised 21 February 2005; accepted 22 February 2005

of optical loss with microdisk radius, along with power dependent measurement of the thermo-optic properties of the microdisks, provide evidence supporting the view that optical loss is dominated in these structures by surface ($5 < R < 20\ \mu$m) and bulk free-carrier absorption ($R > 20\ \mu$m), as opposed to surface roughness on the microdisk. Applications of these devices to nonlinear light scattering, all-optical switching, Si laser resonators, or highly sensitive Si optical sensors are envisioned, where the low loss and tight optical confinement results in extremely large circulating intensities for low optical input powers.

Acknowledgements

This work was supported by DARPA through the EPIC program, and by the Charles Lee Powell Foundation. The authors would like to thank Paul Barclay and Kartik Srinivasan for useful discussions. M.B. thanks the Moore Foundation, NPSC, and HRL Laboratories, and T.J. thanks the Powell Foundation for their graduate fellowship support.

A. Analytic approximation for the modes of a microdisk

Starting with Maxwell's equations for a linear, non-dispersive medium with no free charges or currents,

$$\begin{aligned} \nabla\cdot\mathbf{D}(\mathbf{r},t) &= 0 \qquad & \nabla\times\mathbf{E}(\mathbf{r},t) &= -\frac{\partial\mathbf{B}(\mathbf{r},t)}{\partial t} \\ \nabla\cdot\mathbf{B}(\mathbf{r},t) &= 0 \qquad & \nabla\times\mathbf{H}(\mathbf{r},t) &= \frac{\partial\mathbf{D}(\mathbf{r},t)}{\partial t}, \end{aligned} \tag{10}$$

where $\mathbf{D}(\mathbf{r},t) = \varepsilon(\mathbf{r})\mathbf{E}(\mathbf{r},t)$ and $\mathbf{H}(\mathbf{r},t) = \frac{1}{\mu_o}\mathbf{B}(\mathbf{r},t)$ are the linear constitutive relations. Using the well known series of vector identities, we can rewrite Maxwell's equations for a piecewise homogeneous medium as wave equations:

$$\nabla^2\mathbf{F} - \frac{n^2(\mathbf{r})}{c^2}\frac{\partial^2\mathbf{F}}{\partial t^2} = 0, \tag{11}$$

where $\mathbf{F} = \{\mathbf{E},\mathbf{H}\}$, $c^2 = \frac{1}{\mu_0\varepsilon_0}$, and $n^2(\mathbf{r}) = \frac{\varepsilon(\mathbf{r})}{\varepsilon_0}$. Furthermore, looking for oscillatory solutions of the form: $\mathbf{F}(\mathbf{r},t) = \mathbf{F}(\mathbf{r})\exp(-i\omega t)$, we can write the cylindrical form of the time-independent Maxwell's equations as

$$\left(\frac{\partial^2}{\partial\rho^2} + \frac{1}{\rho}\frac{\partial}{\partial\rho} + \frac{1}{\rho^2}\frac{\partial^2}{\partial\phi^2} + \frac{\partial^2}{\partial z^2} + \left(\frac{\omega}{c}\right)^2 n^2(\mathbf{r})\right)\mathbf{F}(\mathbf{r}) = 0. \tag{12}$$

Note, the real physical fields are given by $\mathrm{Re}[\mathbf{F}(\mathbf{r},t)]$.

In a thin semiconductor microdisk, the high index contrast provides large vertical confinement. This large confinement admits a powerful approximation by effectively reducing the problem to a two-dimensional one. In this case, there are two dominant polarizations labeled as TE (E field parallel to the disk plane) and TM (E field perpendicular to the disk plane), where Eq. (12) becomes scalar in the $\hat{z}$ direction. As a consequence, F_z corresponds to $H_z(E_z)$ for TE(TM) modes. For $\rho < R$, where R is the disk radius, separation of variables can be used to rewrite Eq. (12) as

$$\frac{1}{W}\left(\frac{\partial^2 W}{\partial\rho^2} + \frac{1}{\rho}\frac{\partial W}{\partial\rho} + \frac{1}{\rho^2}\frac{\partial^2 W}{\partial\phi^2}\right) + \frac{1}{Z}\frac{d^2 Z}{dz^2} + k_o^2 n^2(\mathbf{r}) = 0, \tag{13}$$

where $F_z = W(\rho,\phi)Z(z)$ and $k_0 = \omega/c$. Thus we have two differential equations,

#6513 - $15.00 US Received 2 February 2005; revised 21 February 2005; accepted 22 February 2005

$$\left(\frac{\partial^2 W}{\partial \rho^2}+\frac{1}{\rho}\frac{\partial W}{\partial \rho}+\frac{1}{\rho^2}\frac{\partial^2 W}{\partial \phi^2}\right)+k_0^2\bar{n}^2(\rho)W=0 \tag{14}$$

$$\frac{d^2Z}{dz^2}+k_0^2\left(n^2(z)-\bar{n}^2\right)Z=0, \tag{15}$$

to self-consistently solve for the effective index, $\bar{n}$. The solution of Eq. (15) follows the standard slab mode calculations as in [23] taking note that F_z is continuous(discontinuous) across the interfaces for the TE(TM) modes. Equation (14) can be solved by again using separation of variables, $W(\rho,\phi)=\Psi(\rho)\Omega(\phi)$, to rewrite it as:

$$\frac{\partial^2 \Psi}{\partial \rho^2}+\frac{1}{\rho}\frac{\partial \Psi}{\partial \rho}+\left(k_0^2\bar{n}^2(\rho)-\frac{m^2}{\rho^2}\right)\Psi=0 \tag{16}$$

$$\frac{\partial^2 \Omega}{\partial \phi^2}+m^2\Omega=0. \tag{17}$$

While the solution to Eq. (17) is simply $\Omega(\phi)\sim\exp(im\phi)$, the solution to Eq. (16) is most tractably solved approximately [22]. Inside the disk the radial solutions are Bessel functions, $\Psi(\rho)\sim J_m(k_o\bar{n}\rho)$. Outside the disk, the solutions are Hankel functions which can be approximated by a decaying exponential with decay constant $\alpha=k_0(\bar{n}^2-n_0^2)^{1/2}$. The free-space wavelength can then be found by matching the boundary conditions at $\rho=R$ using Eq. (10). Matching $H_z(E_z)$ and E_ϕ for TE(TM) leads to the transcendental equation,

$$k_0\bar{n}(k_0)J_{m+1}(k_0\bar{n}(k_0)R)=\left(\frac{m}{R}+\eta\alpha\right)J_m(k_0\bar{n}(k_0)R), \tag{18}$$

where $\eta=\bar{n}^2/n_0^2$ for TE and unity for TM modes. Using the self-consistent solution of Eq. (15) and Eq. (18), the unnormalized radial mode dependence is given by

$$\Psi(\rho)\sim\begin{cases}J_m(k_0\bar{n}\rho) & \rho\le R\\ J_m(k_0\bar{n}R)\exp\left(-\alpha(\rho-R)\right) & \rho>R\end{cases}. \tag{19}$$

B. Derivation of Q_{ss} from the Volume Current Method

Optical losses in microresonators are often times limited by index perturbations, $\delta\varepsilon$, on the surfaces. These index perturbations are sourced approximately by the unperturbed field solutions, $\mathbf{E}^0$, to create polarization currents,

$$\mathbf{J}=-i\omega\delta\varepsilon\mathbf{E}^0. \tag{20}$$

In analogy with microwave electronics, the polarization currents drive new electromagnetic fields which radiate into space. Optical losses due to the perturbations can be calculated from the far field solutions setup by $\mathbf{J}$ [24] . In most microdisk work, the dominant deviations from the ideal disk geometry occur on the sidewalls during fabrication. Etch-induced sidewall roughness typically runs the height of the disk, providing a nearly one-dimensional way of representing this roughness along the arclength. In this way, the index perturbation (Fig. 1) can be approximated by

$$\delta\varepsilon=\varepsilon_0\delta n^2 h\Delta r(\phi)\delta(r-R)\delta(z), \tag{21}$$

where ε_0 is the free space permittivity, $\delta n^2=n_d^2-n_0^2$, n_d is the disk refractive index, n_0 is the index of the surrounding medium, h is the disk height, and $\Delta r(\phi)$ is the radial surface

#6513 - $15.00 US Received 2 February 2005; revised 21 February 2005; accepted 22 February 2005

roughness relative to the unperturbed disk radius [19]. The parameters ρ, ϕ, and z correspond to the radius from the disk center, angle along the disk perimeter, and height along the disk edge, respectively. The far field vector potential sourced by $\mathbf{J}$ is given by [24]

$$\mathbf{A}_{rad}(\mathbf{r}) = \frac{\mu_o}{4\pi}\left(\frac{e^{-ik_1 r}}{r}\right)\int \mathbf{J}(\mathbf{r}')e^{-ik_1\hat{\mathbf{r}}\cdot\mathbf{r}'}d\mathbf{r}', \tag{22}$$

where $k_1 \equiv n_0 k_0$ is the wave vector in the surrounding medium. Writing the unperturbed electric field at the disk edge as $\mathbf{E}^0 = \mathbf{E}_m(\rho,z)\exp(im\phi)$, Eq. (22) simplifies to

$$\mathbf{A}_{rad}(\mathbf{r}) = \frac{-i\mu_0\omega h\delta n^2\varepsilon_0\mathbf{E}_m(R,0)R}{4\pi}\left(\frac{e^{-ik_1 r}}{r}\right)\int_0^{2\pi}\Delta r(\phi')e^{im\phi'}\exp\left(ik_1 R\sin\theta\cos\phi'\right)d\phi'. \tag{23}$$

For low loss microdisks, the direct solution to Eq. (23) becomes increasingly sensitive to the limitations on the measurement of $\Delta r(s)$, where $s \equiv \phi R$, the arclength along the disk edge perimeter. However, a simple statistical solution becomes possible once surface roughness becomes much smaller than the wavelength in the material [19]. In effect, this simplification assumes that roughness separated by much more than a characteristic correlation length, L_c, is statistically independent. This allows each infinitesimal arclength along the perimeter to be treated as an ensemble member of all the possible processing outcomes under the same fabrication conditions. Ensemble averaging over Eq. (23) yields

$$\left\langle \mathbf{A}_{rad}(\mathbf{r})\cdot\mathbf{A}_{rad}(\mathbf{r})^*\right\rangle = \left|\frac{\mu_0\omega h\delta n^2\varepsilon_0\mathbf{E}_m(R,0)}{4\pi}\right|^2\left(\frac{R}{r}\right)^2\Theta \tag{24}$$

$$\Theta \equiv \int_0^{2\pi}\int_0^{2\pi} C\left(\left|\phi'-\phi''\right|\right)\exp\left(im(\left|\phi'-\phi''\right|\right)\exp\left[ik_1 R\sin\theta\left(\cos\phi'-\cos\phi''\right)\right]d\phi' d\phi'', \tag{25}$$

where $C(|\phi'-\phi''|) = \langle\Delta r(\phi')\Delta r(\phi'')\rangle$, the correlation function for the etch roughness. With the substitutions, $t = \phi'-\phi''$ and $z = (\phi'+\phi'')/2$, the integral is evaluated to be

$$\Theta = 2\pi\int_0^{2\pi} C(t)\exp(imt)J_0\left[2k_1 R\sin\theta\sin\left(\frac{t}{2}\right)\right]dt. \tag{26}$$

With a Gaussian model for the correlation function given by $C(s) = \sigma_R^2\exp\left(-s^2/L_c^2\right)$, this integral becomes

$$\Theta = \frac{2\pi}{R}\int_{-\pi R}^{\pi R}\sigma_R^2\exp\left(-\frac{s^2}{L_c^2}+i\frac{m}{R}s\right)J_0\left[2k_1 R\sin\theta\sin\left(\frac{sR}{2}\right)\right]ds \cong \frac{2\pi^{3/2}\sigma_R^2 L_c}{R}, \tag{27}$$

where σ_R is the standard deviation for the surface roughness. Combining Eqs. (27) and (24), the far field Poynting vector is given by

$$\langle\mathbf{S}_{rad}\rangle = \hat{\mathbf{r}}\frac{\omega k_0}{2\mu_0}\left\langle\left|\hat{\mathbf{r}}\times\mathbf{A}_{rad}\right|^2\right\rangle = \hat{\mathbf{r}}\frac{\omega k_1^3 n_0\left(\delta n^2\right)^2 V_s^2\varepsilon_0\left|\mathbf{E}_m(R,0)\right|^2}{16\sqrt{\pi}}\frac{\left|\hat{\mathbf{r}}\times\hat{\mathbf{e}}\right|^2}{r^2}, \tag{28}$$

where $\hat{\mathbf{e}}$ is the polarization of the electric field and $V_s \equiv \sqrt{RL_c}h\sigma_r$ is the effective volume for a typical scatterer. The total power radiated, P_{rad}, far from the disk can be found by integrating the outward intensity over a large sphere and summing the polarization components to obtain

#6513 - $15.00 US Received 2 February 2005; revised 21 February 2005; accepted 22 February 2005

$$P_{rad} = \int (\mathbf{S}\cdot\hat{\mathbf{r}})\, r^2 d\Omega = \sum_{\hat{\eta}} \frac{\pi^{7/2}\omega n_0 \left(\delta n^2\right)^2 V_s^2 \varepsilon_0 \left|E_m(R,0;\hat{\eta})\right|^2 G(\hat{\eta})}{\lambda_0^3}, \tag{29}$$

where $\hat{\eta} = \{\hat{\rho},\hat{\phi},\hat{\mathbf{z}}\}$ and $G(\hat{\eta}) = \{2/3, 2, 4/3\}$ is a geometrical radiation factor for the different electric field polarizations. Since the quality factor of a cavity mode is given by $Q = \omega U_c / P_{rad}$, where $U_c = \frac{1}{2}\int \varepsilon^0(\mathbf{r}) \left|\mathbf{E}^0\right|^2 d\mathbf{r}$ is the time-averaged stored energy in the cavity, we can rewrite Eq. (29) as a surface scattering quality factor

$$Q_{ss} = \frac{\lambda_o^3}{\pi^{7/2} n_o \left(\delta n^2\right)^2 V_s^2 \sum_{\hat{\eta}} \bar{u_s}(\hat{\eta}) G(\hat{\eta})}, \tag{30}$$

where $\bar{u_s}(\hat{\eta})$ is the normalized, spatially-averaged (see Appendix E) $\hat{\eta}$-polarized electric field energy density at the disk edge given by

$$\bar{u_s}(\hat{\eta}) = \frac{\varepsilon_0 \left|\mathbf{E}^0(\hat{\eta})\right|^2_{s,avg}}{\frac{1}{2}\int \varepsilon^0(\mathbf{r}) \left|\mathbf{E}^0\right|^2 d\mathbf{r}}. \tag{31}$$

Numerical calculations of $\bar{u_s}(\hat{\eta})$ show that TE modes couple to far field radiation modes roughly 50 % more strongly than corresponding TM modes, mainly due to geometrical considerations through $G(\hat{\eta})$. Note that this and the following section has corrected minor errors present in reference [9].

C. Derivation of Q_β via time-dependent perturbation theory

In addition to coupling to radiation modes, surface roughness on microdisks will also couple the degenerate clockwise (*cw*) and counterclockwise (*ccw*) modes [18]. Lifting this degeneracy creates a downshifted- and upshifted-frequency standing wave mode. Based on the work of Gorodetsky, *et al*.[20], a time-dependent perturbation theory can be formulated to quantify this doublet splitting. Then a statistical approach similar to that of Little and Laine [19] can be used to relate the doublet frequency splitting to measured surface roughness. The same polarization currents from Eq. (20) can be added to Eq. (11) to arrive at

$$\nabla^2\mathbf{E} - \mu_0\left(\varepsilon^0 + \delta\varepsilon\right)\frac{\partial^2\mathbf{E}}{\partial t^2} = 0, \tag{32}$$

where $\varepsilon^0(\mathbf{r})$ is the dielectric structure for the ideal disk. The unperturbed modes with an assumed harmonic time dependence, denoted by $\mathbf{E}_j^0(\mathbf{r},t) = \mathbf{E}_j^0(\mathbf{r})\exp(i\omega_j t)$, are a solution of

$$\nabla^2\mathbf{E}_j^0(\mathbf{r}) + \mu_0\varepsilon^0(\mathbf{r})\omega_j^2\mathbf{E}_j^0(\mathbf{r}) = 0. \tag{33}$$

Now assuming slowly varying envelopes $a_j(t)$, the perturbed modes are given by

$$\mathbf{E}(\mathbf{r},t) = \exp(-i\omega_0 t)\sum_j a_j(t)\mathbf{E}_j^0(\mathbf{r}). \tag{34}$$

Substituting Eq. (34) into Eq. (32) and keeping terms to first order yields

$$\sum_j \left(2i\omega_0\varepsilon^0\frac{da_j}{dt} + \delta\varepsilon\omega_0^2 a_j - \varepsilon^0(\omega_j^2 - \omega_0^2)a_j\right)\mathbf{E}_j^0(\mathbf{r}) = 0. \tag{35}$$

Using the fact that $\int \varepsilon^0 \left(\mathbf{E}_j^0(\mathbf{r})\right)^* \mathbf{E}_k^0(\mathbf{r}) d\mathbf{r} = 0$ for $j \neq k$ (shown in Ref. [29]), Eq. (35) can be multiplied by $\left(\mathbf{E}_j^0(\mathbf{r})\right)^*$ and integrated over all space to obtain

#6513 - $15.00 US Received 2 February 2005; revised 21 February 2005; accepted 22 February 2005

$$\frac{da_k}{dt} + i\Delta\omega_k a_k(t) = i\sum_j \beta_{jk} a_j, \tag{36}$$

$$\text{with } \beta_{jk} = \frac{\omega_0}{2} \frac{\int \delta\varepsilon \left(\mathbf{E}_j^0(\mathbf{r})\right)^* \mathbf{E}_k^0(\mathbf{r}) d\mathbf{r}}{\int \varepsilon^0 \left|\mathbf{E}_k^0(\mathbf{r})\right|^2 d\mathbf{r}}, \tag{37}$$

where $\Delta\omega_k = \omega_k - \omega_0$. The radius of the ideal disk in $\varepsilon^0(\mathbf{r})$ is chosen as the average radius of the perturbed disk so as to work in a basis where the strength of the perturbation does not create a self-term frequency shift (i.e., $\beta_{jj} = 0$). For the case of initially degenerate *cw* and *ccw* modes, we can take this coupled mode formalism and resonantly pump the system with an external waveguide. For small perturbations, we can assume that the backscattering rate for each mode is identical, $\beta_{cw,ccw} = \beta_{ccw,cw} \equiv \beta$. When all other modes are far off-resonance, the coupled mode equations then become symmetrically

$$\frac{da_{cw}}{dt} = -i\Delta\omega a_{cw} + i\beta a_{ccw} \tag{38a}$$

$$\frac{da_{ccw}}{dt} = -i\Delta\omega a_{ccw} + i\beta a_{cw}, \tag{38b}$$

where $\Delta\omega_{cw} = \Delta\omega_{ccw} \equiv \Delta\omega$. A functional form for β can be analytically derived for small amounts of etch roughness. Substituting the delta function approximation for the dielectric perturbation from Eq. (21), we obtain

$$\beta = \frac{\omega_0}{4U_c} \int \varepsilon_0 \delta n^2 h \Delta r(s) \delta(r-R) \delta(z) \left(\mathbf{E}_{cw}(\mathbf{r})\right)^* \mathbf{E}_{ccw}(\mathbf{r}) d\mathbf{r}. \tag{39}$$

This integral is easily reduced to a Fourier-type integral by noting that at the disk edge $\mathbf{E}_{cw} = \mathbf{E}_m(R,0)\exp(-im\phi)$ and $\mathbf{E}_{ccw} = \mathbf{E}_m(R,0)\exp(im\phi)$. Integrating over the δ-functions yields

$$\beta = \frac{\omega_0 \delta n^2 h R \varepsilon_0 \left|\mathbf{E}_m(R,0)\right|^2}{4U_c} \Upsilon \tag{40}$$

$$\Upsilon = \int_0^{2\pi} \Delta r(\phi) e^{i2m\phi} d\phi. \tag{41}$$

As in Eq. (23), the integral, Υ, becomes statistically solvable when surface roughness becomes much smaller than the wavelength in the material. Following the same method of solution and definitions as above,

$$\left\langle \Upsilon^2 \right\rangle = \frac{2\pi}{R} \int_{-\pi R}^{\pi R} \sigma_R^2 \exp\left(-\frac{s^2}{L_c^2} + i\frac{2m}{R}s\right) \cong \frac{2\pi^{3/2}\sigma_R^2 L_c}{R}. \tag{42}$$

Plugging Eq. (42) into Eq. (40) and solving gives $\sqrt{\langle\beta^2\rangle} = (\pi/4)^{3/4} \omega_0 \delta n^2 V_s \bar{u}_s$, where $\bar{u}_s \equiv \sum_{\hat{\eta}} \bar{u}_s(\hat{\eta})$. To model coupling power into this resonant system, a phenomenological loss rate, $\gamma_t \equiv \omega/Q_t$, and a coupling coefficient, κ, can be added to obtain, [21]

$$\frac{da_{cw}}{dt} = -\left(\frac{\gamma_t}{2} + i\Delta\omega\right) a_{cw} + i\beta a_{ccw} + \kappa s \tag{43a}$$

$$\frac{da_{ccw}}{dt} = -\left(\frac{\gamma_t}{2} + i\Delta\omega\right) a_{ccw} + i\beta a_{cw}, \tag{43b}$$

#6513 - $15.00 US Received 2 February 2005; revised 21 February 2005; accepted 22 February 2005

where a_j are normalized energy amplitudes, $|s|^2$ is the normalized input power, and $\gamma_t = \gamma_e + \gamma_i'$. The loss rate can been broken down into loss from the cavity back into the waveguide, γ_e, and all other loss, γ_i'. Assuming the coupling itself is lossless and obeys time reciprocity, a scattering matrix formalism can further show that $\kappa^2 = \gamma_e$[30]. Additionally, the transmitted and reflected powers are given by [21] $|t|^2 = |-s + \kappa a_{cw}|^2$ and $|r|^2 = |\kappa a_{ccw}|^2$. Steady-state solutions of Eqs. (43a) and (43b) show transmission dips at $\omega = \omega_0 \pm \beta$. Thus, a normalized measure of the backscattering rate is defined to be the natural frequency divided by the *total* resonance splitting, $Q_\beta \equiv \omega_0/(2\beta)$:

$$Q_\beta = \frac{\sqrt{2}}{\pi^{3/4}\delta n^2 V_s \bar{u_s}}. \tag{44}$$

D. Derivation of Q_{sa}

In contrast to surface scattering, surface *absorption* resulting from lattice reconstructions is also present as a source of optical loss. Since great care is taken to preserve the quality of the top and bottom surfaces of the silicon microdisk, it is reasonable to assume that the dominant lattice damage occurs at the disk sidewalls during the etch. While efforts are taken to minimize etch damage, it remains clear that reactive ion etching locally damages the lattice during the material ablation allowing for the incorporation of various lattice impurities and defects [15]. The local surface absorption rate coefficient, $\gamma_{sa}(\mathbf{r})$, is used to calculate a spatially-averaged loss coefficient according to:

$$\bar{\gamma}_{sa} = \frac{\int \gamma_{sa}(\mathbf{r}) n^2(\mathbf{r}) |E(\mathbf{r})|^2 d\mathbf{r}}{\int n^2(\mathbf{r}) |E(\mathbf{r})|^2 d\mathbf{r}}, \tag{45}$$

where the appropriate weighting function is proportional to the electric field energy density of the optical mode [16]. An approximate model for $\gamma_{sa}(\mathbf{r})$ would be to assume that their exists a reconstruction depth, ζ, where the loss rate is a constant γ_{sa} and zero elsewhere. Thus, the electric field in the numerator of Eq. (45) is approximately constant over a cylindrical shell with volume $\delta V_{sa} = 2\pi R\zeta h$. By using Eq. (31) and assuming that the surface reconstruction has approximately the same index of refraction as that of the undisturbed lattice [15], we have

$$\bar{\gamma}_{sa} = \gamma_{sa} n_{\mathrm{Si}}^2 \frac{\int_{\delta V_{sa}} |E(\mathbf{r})|^2 d\mathbf{r}}{\int n^2(\mathbf{r}) |E(\mathbf{r})|^2 d\mathbf{r}} = \frac{1}{2}\gamma_{sa} n_{\mathrm{Si}}^2 \bar{u_s} \delta V_{sa}. \tag{46}$$

Defining $Q_{sa} = \omega/\bar{\gamma}_{sa}$, we can then write for the surface-absorption quality factor

$$Q_{sa} = \frac{4\pi c}{\lambda_0 \gamma_{sa} n_{\mathrm{Si}}^2 \bar{u_s} \delta V_{sa}}. \tag{47}$$

E. Approximate form for the TM case

Considering the TM case only, the normalized disk-edge energy density, $\bar{u}_s(\hat{\mathbf{z}})$ (defined in Eq. (31)), may be estimated analytically for low radial numbers [20]. Having an approximate form for $\bar{u_s}(\hat{\mathbf{z}})$ is extremely important if we are to develop intuition from the previous results. As an approximation to the actual (unperturbed) normalized disk-edge energy density for all points within the disk-edge perturbations, an average value over a thin cylindrical shell is used. Defining the peak radial amplitude of the roughness to be δr, the averaged intensity is given by

$$|\mathbf{E}|^2_{s,avg} = \frac{1}{\delta V} \int_{R-\delta r}^{R+\delta r} \int_{-h/2}^{h/2} \int_0^{2\pi} \rho d\rho d\phi dz |\mathbf{E}|^2, \tag{48}$$

#6513 - $15.00 US Received 2 February 2005; revised 21 February 2005; accepted 22 February 2005

where $\delta V = 4\pi\delta r R h$. Note that while surface absorption reconstruction depth does not necessarily correlate with surface roughness amplitude, this mathematical formalism is identical with $\zeta = 2\delta r$. For high index contrast structures, the cavity mode energy can be approximated as existing only inside the cavity. Therefore we have,

$$U_c = \frac{1}{2}\int \varepsilon^0(\mathbf{r})\,|\mathbf{E}|^2\,d\mathbf{r} \approx \frac{1}{2}\varepsilon_0 n_d^2 \int_0^R \int_{-h/2}^{h/2}\int_0^{2\pi} \rho\, d\rho\, d\phi\, dz\,|\mathbf{E}|^2\,. \tag{49}$$

Since the ϕ and z integrations in Eqs. (48) and (49) are identical, only the radial integrals need to be considered. Since $\mathbf{E} \sim J_m(k_0\bar{n}\rho)$, we can write

$$\bar{u_s}(\hat{\mathbf{z}}) = \frac{2}{n_d^2\delta V}\frac{\int_{R-\delta r}^{R+\delta r}\rho\, d\rho\,[J_m(k_0\bar{n}\rho)]^2}{\int_0^R \rho\, d\rho\,[J_m(k_0\bar{n}\rho)]^2}. \tag{50}$$

As an alternative to solving Eq. (50) numerically, a closed form expression can be obtained by reintroducing the δ-function approximation for the radial integral over the thin shell. Using several Bessel identities along with the continuity conditions for Maxwell's equations, Eq. (50) can be reduced to

$$\bar{u_s}(\hat{\mathbf{z}}) = \frac{[J_m(k_0\bar{n}R)]^2}{\pi h n_d^2 \int_0^R \rho\, d\rho\,[J_m(k_0\bar{n}\rho)]^2} \approx \frac{2\bar{n}^2}{V_d n_d^2\left(\bar{n}^2 - n_0^2\right)}, \tag{51}$$

where $V_d = \pi R^2 h$. This approximate form for $\bar{u_s}(\hat{\mathbf{z}})$ shows that the sensitivity to the disk edge decreases as the radius of the disk is increased. Substituting Eq. (51) into Eqs. (30,44,47) gives the working equations for the analysis presented in the main text of this paper:

$$Q_{ss} = \frac{3\lambda_0^3}{8\pi^{7/2} n_0 \delta n^2 \xi}\left(\frac{V_d}{V_s^2}\right), \tag{52}$$

$$Q_\beta = \frac{1}{\sqrt{2}\pi^{3/4}\xi}\left(\frac{V_d}{V_s}\right), \tag{53}$$

$$Q_{sa} = \frac{\pi c\left(\bar{n}^2 - n_0^2\right)R}{\lambda_0 \bar{n}^2 \gamma_{sa}\zeta}, \tag{54}$$

where a relative dielectric contrast constant ξ is defined to be

$$\xi = \frac{\bar{n}^2\left(n_d^2 - n_0^2\right)}{n_d^2\left(\bar{n}^2 - n_0^2\right)}. \tag{55}$$

#6513 - $15.00 US Received 2 February 2005; revised 21 February 2005; accepted 22 February 2005